

GL-TR-89-0316

PROGRAM TO PERFORM RESEARCH ON USE OF LIDAR FOR RANGE  
RESOLVED TURBULENCE MEASUREMENTS

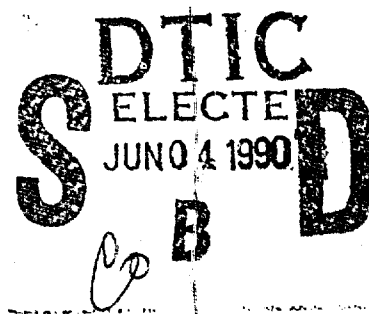
Warren P. Moskowitz  
Richard C. Garner

AD-A222 189

PhotoMetrics, Inc.  
4 Arrow Drive  
Woburn, MA 01801

30 November 1989

Final Report  
23 September 1988 - 30 October 1989



Approved for public release; distribution unlimited.

GEOPHYSICS LABORATORY  
AIR FORCE SYSTEMS COMMAND  
UNITED STATES AIR FORCE  
HANSOM AFB, MASSACHUSETTS 07131-5000

90 05 31 068

"This technical report has been reviewed and approved for publication"

James H. Brown  
(Signature)  
James H. Brown  
Contract Manager

Donald E. Bede  
(Signature)  
Donald E. Bede, Chief  
Atmospheric Optics Branch

FOR THE COMMANDER

R. Earl Good  
(Signature)  
R. Earl Good, Director  
Optical and Infrared Technology Division

This report has been reviewed by the ESD Public Affairs Office (PA) and is releasable to the National Technical Information Service (NTIS).

Qualified requestors may obtain additional copies from the Defense Technical Information Center. All others should apply to the National Technical Information Service.

If your address has changed, or if you wish to be removed from the mailing list, or if the addressee is no longer employed by your organization, please notify GL/IMA, Hanscom AFB, MA 01731. This will assist us in maintaining a current mailing list.

Do not return copies of this report unless contractual obligations or notices on a specific document requires that it be returned.

**Unclassified**

SECURITY CLASSIFICATION OF THIS PAGE

## REPORT DOCUMENTATION PAGE

|   |  |  |  |                              |                                  |
|---|--|--|--|------------------------------|----------------------------------|
| 1a. REPORT SECURITY CLASSIFICATION<br><b>Unclassified</b>   |  | 1b. RESTRICTIVE MARKINGS   |  |                              |                                  |
| 2a. SECURITY CLASSIFICATION AUTHORITY   |  | 3. DISTRIBUTION/AVAILABILITY OF REPORT<br>Approved for public release;<br>distribution unlimited.                                      |  |                              |                                  |
| 2b. DECLASSIFICATION/DOWNGRADING SCHEDULE<br>N/A  |  |  |  |                              |                                  |
| 4 PERFORMING ORGANIZATION REPORT NUMBER(S)<br>PhM-TR-89-10  |  | 5. MONITORING ORGANIZATION REPORT NUMBER(S)<br>GL-TR-89-0316   |  |                              |                                  |
| 6a. NAME OF PERFORMING ORGANIZATION<br>PhotoMetrics, Inc.   | 6b. OFFICE SYMBOL<br>(If applicable)       | 7a. NAME OF MONITORING ORGANIZATION<br>Geophysics Laboratory   |  |                              |                                  |
| 6c. ADDRESS (City, State, and ZIP Code)<br>4 Arrow Drive<br>Woburn, MA 01801  |  | 7b. ADDRESS (City, State, and ZIP Code)<br>Hanscom AFB<br>Massachusetts 01731-5000   |  |                              |                                  |
| 8a. NAME OF FUNDING/SPONSORING<br>ORGANIZATION  | 8b. OFFICE SYMBOL<br>(If applicable)       | 9. PROCUREMENT INSTRUMENT IDENTIFICATION NUMBER<br>F19628-88-C-0150  |  |                              |                                  |
| 8c. ADDRESS (City, State, and ZIP Code)   |  | 10. SOURCE OF FUNDING NUMBERS  |  |                              |                                  |
|   |  | PROGRAM<br>ELEMENT NO.<br>61101F   | PROJECT<br>NO.<br>ILIR                               | TASK<br>NO.<br>8I            | WORK UNIT<br>ACCESSION NO.<br>AA |
| 11. TITLE (Include Security Classification)<br>PROGRAM TO PERFORM RESEARCH ON USE OF LIDAR FOR RANGE RESOLVED TURBULENCE<br>MEASUREMENTS  |  |  |  |                              |                                  |
| 12. PERSONAL AUTHOR(S)<br>Warren P. Moskowitz, Richard C. Garner  |  |  |  |                              |                                  |
| 13a. TYPE OF REPORT<br>Final Technical  | 13b. TIME COVERED<br>FROM 880928 TO 891030 | 14. DATE OF REPORT (Year, Month, Day)<br>891130  |  | 15. PAGE COUNT<br>42         |                                  |
| 16. SUPPLEMENTARY NOTATION  |  |  |  |                              |                                  |
| 17. COSATI CODES  |  | 18. SUBJECT TERMS (Continue on reverse if necessary and identify by block number)<br>Atmospheric Turbulence, Lidar, Optical Turbulence |  |                              |                                  |
| FIELD   | GROUP                                      | SUB-GROUP  |  |                              |                                  |
| 19. ABSTRACT (Continue on reverse if necessary and identify by block number)<br>The design of a lidar system capable of measuring remotely range-resolved atmospheric turbulence is presented. The connection between the measured quantities and the accepted turbulence strength parameter ( $C_n^2$ ) is developed theoretically. Simulations of an operating system have been made, and the results provide a measure of system capability. A typical value for ( $C_n^2$ ) of $10^{-16} \text{ m}^{-2}$ at 3 km vertical range is measurable with a 200 m range resolution. (See $\sigma_{\ln I}$ .) |  |  |  |                              |                                  |
| 19. ABSTRACT (Continuation of previous block)<br>The design of a lidar system capable of measuring remotely range-resolved atmospheric turbulence is presented. The connection between the measured quantities and the accepted turbulence strength parameter ( $C_n^2$ ) is developed theoretically. Simulations of an operating system have been made, and the results provide a measure of system capability. A typical value for ( $C_n^2$ ) of $10^{-16} \text{ m}^{-2}$ at 3 km vertical range is measurable with a 200 m range resolution. (See $\sigma_{\ln I}$ .)                                |  |  | C sub n = -59  |                              |                                  |
| 20. DISTRIBUTION/AVAILABILITY OF ABSTRACT<br><input type="checkbox"/> UNCLASSIFIED/UNLIMITED <input checked="" type="checkbox"/> SAME AS RPT. <input type="checkbox"/> DTIC USERS   |  |  | 21. ABSTRACT SECURITY CLASSIFICATION<br>Unclassified |                              |                                  |
| 22a. NAME OF RESPONSIBLE INDIVIDUAL<br>Mr. James H. Brown, Contract Manager   |  |  | 22b. TELEPHONE (Include Area Code)<br>617/377-4412   | 22c. OFFICE SYMBOL<br>GL/OPA |                                  |

SECURITY CLASSIFICATION OF THIS PAGE

SECURITY CLASSIFICATION OF THIS PAGE

**Forward**

This report covers PhotoMetrics' one year effort under Contract F19628-88-C-0150 to perform research on the application of lidar techniques to the measurement of range resolved atmospheric turbulence. The authors wish to thank Mr. James H. Brown (GL/OPA), the Contract Manager, for his support throughout the program.



| Accession For       |                                     |
|---------------------|-------------------------------------|
| NTIS GRA&I          | <input checked="" type="checkbox"/> |
| DTIC TAB            | <input type="checkbox"/>            |
| Unannounced         | <input type="checkbox"/>            |
| Justification       |                                     |
| By _____            |                                     |
| Distribution/ _____ |                                     |
| Availability Codes  |                                     |
| Dist                | Avail and/or<br>Special             |
| A-1                 |                                     |

# Contents

|   |     |
|---|-----|
| <b>Forward</b>  | iii |
| <b>Table of Contents</b>  | iv  |
| <b>List of Figures</b>  | vi  |
| <b>1 Introduction</b>   | 1   |
| 1.1 Objective . . . . .   | 1   |
| 1.2 Organization . . . . .                                      | 1   |
| <b>2 Progress</b>   | 2   |
| 2.1 First half . . . . .  | 2   |
| 2.2 Second half . . . . .                                       | 2   |
| <b>3 Brief description</b>                                      | 3   |
| 3.1 Deconvolution scheme . . . . .                              | 4   |
| 3.2 Bending moment scheme . . . . .                             | 4   |
| <b>4 Experimental work</b>                                      | 5   |
| <b>5 Relationship of angle of arrival to <math>C_n^2</math></b> | 9   |
| <b>6 Range resolved <math>C_n^2</math></b>                      | 12  |
| 6.1 Forward and Backscattered Paths . . . . .                   | 12  |
| 6.2 Deconvolution method . . . . .                              | 13  |
| 6.2.1 Description . . . . .                                     | 13  |
| 6.2.2 Examples . . . . .  | 14  |
| 6.3 Bending moment method . . . . .                             | 14  |
| 6.3.1 Description . . . . .                                     | 14  |
| 6.3.2 Examples . . . . .  | 16  |
| 6.4 Errors and Uncertainties . . . . .                          | 18  |
| 6.4.1 Statistical Nature of Turbulence Model . . . . .          | 18  |
| 6.4.2 Nonzero Spot Size . . . . .                               | 19  |
| 6.4.3 Correlation of paths (Isoplanatism) . . . . .             | 20  |
| 6.4.4 Minimum Measureable $C_n^2$ . . . . .                     | 22  |

|   |           |
|---|-----------|
| <b>7 Proposed Range Resolved System</b>     | <b>28</b> |
| <b>7.1 Introduction . . . . .</b>           | <b>28</b> |
| <b>7.2 Transmitter . . . . .</b>            | <b>28</b> |
| <b>7.3 Receivers . . . . .</b>              | <b>30</b> |
| <b>7.4 Tilted image plane . . . . .</b>     | <b>31</b> |
| <b>7.5 Detectors . . . . .</b>              | <b>33</b> |
| <b>7.5.1 Detector Resolution . . . . .</b>  | <b>34</b> |
| <b>7.6 Processing electronics . . . . .</b> | <b>35</b> |
| <b>8 Conclusions</b>                        | <b>35</b> |
| <b>References</b>                           | <b>36</b> |

## List of Figures

|    |   |    |
|----|---|----|
| 1  | Experimental setup. . . . .   | 6  |
| 2  | Experimental data. An intensity profile is determined along the line drawn through the beams. . . . .   | 7  |
| 3  | $C_n^2$ analysis of experimental data with a simultaneous thermosonde comparison . . . . .  | 8  |
| 4  | Turbulence induced wave tilt of backscattered light. . . . .  | 10 |
| 5  | Deconvolution method sample calculation with $C_n^2(z) \propto z^{-4/3}$ . The retrieved and model $C_n^2$ profiles are the same. "AOA" means angle of arrival. . . . .                       | 15 |
| 6  | Bending moment method sample calculation for 100 laser pulses with $C_n^2(z) \propto z^{-4/3}$ . a) Generated and actual $C_n^2(z)$ . b) Simulated $\theta(z)$ for five laser pulses. . . . . | 17 |
| 7  | Isoplanatic angle for $C_n^2 = z^{-4/3} \times (10^{-13} \text{m}^{2/3})$ and angular path difference of two paths backscattered from 3 km. . . . .   | 21 |
| 8  | Sample calculation with $C_n^2(z) \propto z^{-4/3}$ . A (ten times) Raleigh atmosphere is assumed. Spot centroid location uncertainty and isoplanatism are included. . . . .                  | 23 |
| 9  | Minimum measureable $C_n^2$ versus range for 60 m range resolution and two aperture diameters: a) 60 cm and b) 100 cm. . . . .  | 25 |
| 10 | Minimum measureable $C_n^2$ versus range for 60 cm aperture diameter and two range resolutions: a) 100 m and b) 200 m. . . . .  | 26 |
| 11 | Minimum measureable $C_n^2$ versus range for 100 cm aperture diameter and two range resolutions: a) 100 m and b) 200 m. . . . .   | 27 |
| 12 | Proposed system. . . . .  | 29 |
| 13 | Tilted image plane telescope. . . . .   | 32 |

# **1 Introduction**

## **1.1 Objective**

The objective of this program was to perform research leading to the development of a bistatic lidar to measure range-resolved atmospheric turbulence. The strategy has been to use the tilts of the backscattered wavefronts as a measure of the turbulence.

The research consisted of experimental and theoretical components. The experimental work concerned the measurement of turbulence effects with scaled-down versions of a final design apparatus. Aspects of the design have been adjusted to optimize the sensitivity of the instrument. We have undertaken the theoretical research to assist in the instrument design, and to develop the analysis techniques which would be used on actual data.

## **1.2 Organization**

The rest of this report describes our theoretical and experimental research. This work has lead to the design of a lidar system capable of measuring a  $C_n^2$  value of  $10^{-16} \text{ m}^{-2/3}$  at 3 km vertical range.

Section 2 gives an overview of our work roughly in chronological order. Section 3 gives a brief description of the conceptual background of a  $C_n^2$  measuring lidar.

The rest of the report describes the three aspects of our work:

- 1. Experiments to test the feasibility of measuring the wander (or angle of arrival) of a laser beam backscattered from the atmosphere (Section 4),**
- 2. theory to determine how to extract  $C_n^2$  as a function of range from angle of arrival measurements (Sections 5 and 6), and**
- 3. simulations, using theory with estimates of errors and uncertainties, to design a final system (Sections 6 and 7).**

## **2 Progress**

### **2.1 First half**

During the first six months of this program, our initial concepts for a remote turbulence measuring device were analyzed in depth, both theoretically and experimentally. The overall concept, a bistatic lidar to measure beam wander, was shown to be a viable solution. Our proposed use of homodyne detection to measure the wander angles was abandoned in favor of direct imaging. Direct imaging is a more straightforward technique which is now applicable to this problem due to advances in imaging detector technology.

Experimental work during the first six months primarily involved verification that the turbulence effects can be separated into wander and broadening, and that the experimental parameters can be chosen to maximize the ratio of the former to the latter. The experiments were motivated by a gap in the turbulence literature surrounding beam wander. The summarized data from these experiments are presented in a video tape. The data demonstrate dramatically the beam wander effect.

In the video tape, a laser beam, focussed through a four meter path in the laboratory, is imaged on a Reticon array. A hot air blower (heat gun) provides turbulence over the path. The image, which appeared to the eye to be a blurred or broadened spot, is shown to be a small moving spot when examined in stop motion. At the highest levels of turbulence, the moving spot itself distorts and broadens.

This dominance of wander over broadening is important for the success of any implementation of our turbulence measuring technique. The detector will measure the centroid of the apparent position of the backscattered lidar return versus altitude. The determination of the centroid is rendered less accurate as the beam broadens.

### **2.2 Second half**

We have simulated the performance of a field system using a scaled-down, fixed range, imaging lidar system. The system was used to test the properties of the various components. Simultaneously, we developed a scheme to extract  $C_n^2$  from

the measured data.

Analyzed measurements have been presented and appear in this report. Two thermosondes were operated in the same corridor as the lidar. The thermosonde measurements are presented in figure 3 (on page 8) along with those of the lidar. There is only partial agreement between the two data sets. This has been explained there by the difference in the air volumes sampled by the two techniques (the lidar gives a path weighted average of  $C_n^2$  while the thermosonde gives a point value), and the relatively short period of 120 seconds over which the measurements were made.

The remainder of the work has been mainly computer modeling and simulation. We have modeled the operation of a larger, time resolved lidar system. The experimental errors were included, and the minimum resolvable  $C_n^2$  was determined.

Two schemes had arisen by which  $C_n^2$  could be extracted from the measurements. They differ in the order in which data from individual laser shots are summed and processed. The "deconvolution" scheme processes after summing. The "bending moment" scheme processes before summing. Both methods received detailed examination and modeling, the results of which are presented in this report. Although the bending moment scheme is the more appealing of the two, it was shown to be inapplicable to a backscatter lidar. The results of the bending moment work are presented here in the hope that an application can be found.

### 3 Brief description

We present here a brief description of the turbulence lidar concept. Sections 5 and 6 will give more detail of the theoretical basis of this concept.

A low divergence, short pulse, laser beam is transmitted upward into the atmosphere. A long focal length receiver telescope collects the light which scatters backward and projects an image of the beam on a time resolved imaging detector.

The upward beam and the backscattered light will experience angular deviations as they travel through the turbulent atmosphere. If the image of each laser shot is time resolved at the 100 ns level, the deviation can be recorded for each 15 m interval of travel. The deviation, in the form of a one or two dimensional angular

coordinate is sensed by the detector, digitized by the processing electronics, and fed to a computer. This is the point at which the two  $C_n^2$  extraction techniques begin to differ.

### 3.1 Deconvolution scheme

If the square of the angular deviation is summed for successive laser shots, the result is the mean square deviation as a function of range  $z$ . By angular deviation, we mean the amount by which the image of the beam has moved relative to the image which would have resulted in the absence of turbulence. The angular deviation will be denoted as  $\bar{\theta}$  and the mean square deviation is  $\langle \theta^2 \rangle$ .

Since misalignment or angular instability of the laser transmitter are a possibility, two receivers would be used. The difference between the  $\bar{\theta}$  measurements, is used in place of  $\bar{\theta}$  above. This configuration also cancels the beam wander of the outgoing transmitter beam (which is necessary for our inversion technique to be described). However, it does not avoid the possibility of nonzero correlation between the two backscattered paths. We discuss the correlation in more detail in Section 6 and take it to be zero here. In the following discussion,  $\bar{\theta}$  may be assumed to be the difference measurement although no explicit mention is made of two receivers.

The values of  $\langle \theta^2(z) \rangle$  are predicted by the turbulence theory for any distribution of  $C_n(z)$  (where  $z$  is the range). As explained in section 6,  $\langle \theta^2(z) \rangle$  is an integral from the receiver to  $z$  of  $C_n^2(z)$  times another function. Since the object of the measurement is  $C_n(z)$ , a deconvolution has to be performed.

The deconvolution is calculated as a matrix for a given experimental configuration and multiplied by the array of  $\langle \theta^2(z) \rangle$  values. The usual concern about deconvolutions is their troublesome instability in the presence of experimental noise. Examples given in section 6 show this deconvolution to be fairly well behaved in the presence of modeled experimental error.

### 3.2 Bending moment scheme

As the light beam propagates through the atmosphere, its direction is randomly kicked off course by the refractive index gradients. The kicks add in the usual

random walk way with the strength and direction of the kicks, as well as the distance between kicks varying randomly. This bending moment scheme attempts to extract kick strength or bending moment versus range for each laser shot, and sum successive shots to find the mean square bending moment versus range.

The beauty of this scheme lies in the direct proportionality of the mean square bending moment to  $C_n^2(z)$ . Unfortunately, the algorithm to extract the bending moment from the data is a noise enhancing process. The degree of noise amplification increases dramatically as the range resolution of the final  $C_n^2(z)$  distribution is made finer. The noise is diminished by averaging over many laser shots.

## 4 Experimental work

The first half of this program was spent verifying the utility of beam wander observations as a measurement of turbulence. We spent the final half simulating a measurement system and refining the experimental technique.

The simulation used a fixed focus lidar transmitter and imaging receiver. The focus was at a range of 50 m along a low angle slant path emerging from PhotoMetrics' building. The return was not time resolved — the imaging receiver resolved range geometrically.

We have assumed for these experiments that  $C_n^2$  is constant along the 50 m path. Thus, the statistical characteristics of the beam wander along the forward and backscattered paths are assumed to be the same. If we further assume no correlation between forward and backscattered paths, the expected beam wander should be that for a 100 m path with the same constant  $C_n^2$ .

If  $C_n^2$  is not constant then  $C_n^2$  calculated from measurements made with this system corresponds to a weighted average of  $C_n^2$  over the 50 m path. The weighting function is given by Equations 3 to 5 in the Section 5.

Figure 1 shows our experimental setup. The laser is a single spatial mode, doubled Nd:YAG operating at 5 kHz pulse rate and 60  $\mu$ J/pulse. The laser beam is split, with part of the beam spatially shifted by 0.25 millimeters. Both parts are expanded to 5 cm and focused at 50 m. Their lateral separation at the focus is 2.5 cm.

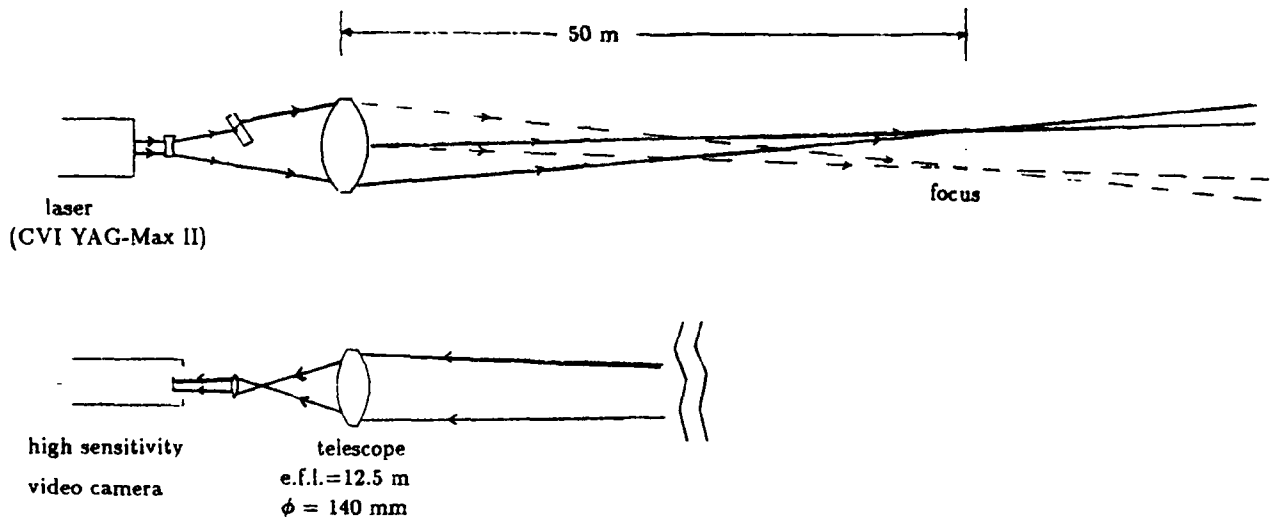


**Figure 1: Experimental setup.**

To negate beam wander induced in the laser we measure the difference in angles of arrival of the two beams backscattered to one receiver. This is in contrast to our proposed range resolved lidar system which incorporates two receivers and one transmitter beam. As we mentioned in Section 3, the proposed system must have beam wander along the forward path negated as well. This cannot be achieved with single receiver.

The receiver consists of a 12.5 m effective focal length telescope with a 140 mm diameter aperture, followed by a high sensitivity Cohu intensified (ISIT) video camera. The two backscattered beams are imaged simultaneously onto the video camera active area. The camera output is monitored in real time and recorded on video tape.

Figure 2 shows a typical video frame of data. One frame consists of backscattered light collected during a 1/30 second time interval. The centers of the two beams at the focus are approximately 194 pixels apart, corresponding to 445  $\mu$ rad. We acquire such video data for several minutes. The two beams wander relative to

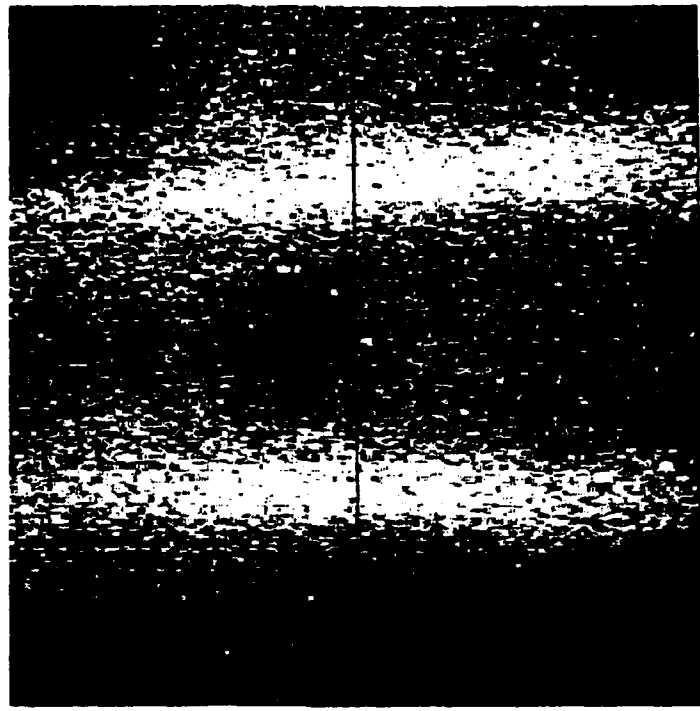


**Figure 2:** Experimental data. An intensity profile is determined along the line drawn through the beams.

each other randomly due to the turbulence along the path. Typical wander is on the order of a few pixels, corresponding to a few microradians. The variance of the beam wander is proportional to  $C_n^2$ , as we show in the theory section of this report.

We analyzed the video data using a digital image analyzer (Datacube MaxVision AT-1) connected to an 80386 based computer. Our analysis of the data consisted of grabbing 3600 frames of data, determining the pixel intensity profiles along a line perpendicular to the two beams at the focus, and numerically autocorrelating the profile to determine the beam separation for each frame.

The results of this data analysis, with a thermosonde comparison, are shown in figure 3. The upper curve shows  $C_n^2$  derived from laser measurements. Each  $C_n^2$  value is calculated by considering the variance of angles of arrival for 150 video frames (5 sec of data). Equation 6 in the next section is assumed to be the relationship between  $C_n^2$  and angle of arrival variance (the relationship for constant  $C_n^2$ ).

The lower curve shows  $C_n^2$  derived from measurements taken with a thermosonde.

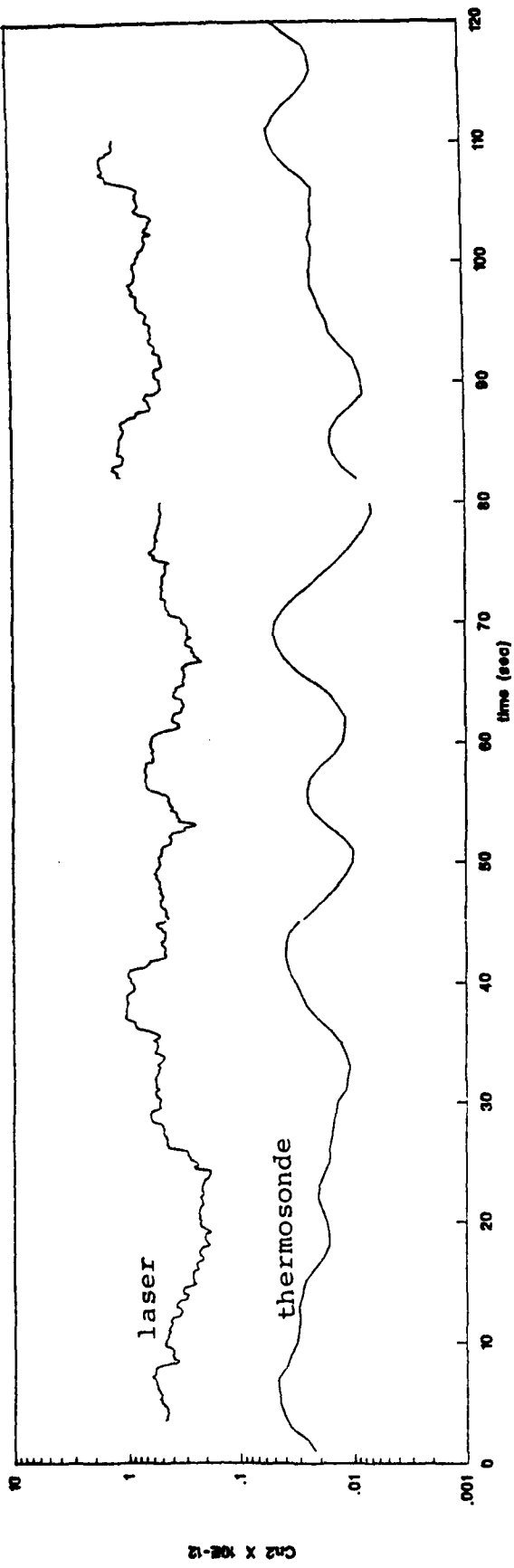


Figure 3:  $C_n^2$  analysis of experimental data with a simultaneous thermosonde comparison

The thermosonde was located approximately 4 m from the laser/receiver along the propagation path, separated by a radial distance of 10 cm. Data from the thermosonde was acquired at a rate of  $1 \text{ sec}^{-1}$ . Five seconds of data were averaged to compute  $C_n^2$ . The thermosonde measures the value  $C_T^2$ . We calculate  $C_n^2$  using the relation [1]

$$C_n^2 = \left( \frac{79P}{T^2} \times 10^{-6} \right)^2 C_T^2 \quad (1)$$

where P is the pressure in millibars and T is the temperature in degrees Kelvin.

The partial correlation of the two sets of data is encouraging. A lack of correlation is expected for several reasons:

1. The laser provides a path weighted average of  $C_n^2$  whereas the thermosonde provides a point measurement,
2. turbulence along the forward and backscattered paths may be correlated, leading to a more complicated inversion scheme, and
3. the thermosonde was slightly removed from the laser path.

Therefore, partial correlation indicates that the measured effect (backscattered beam motion) is indicative of turbulence induced beam wander. A more thorough experimental setup (one outside the scope of this work) would be necessary to test for correlation between the lidar technique of measuring  $C_n^2$  and other, proven, techniques.

## 5 Relationship of angle of arrival to $C_n^2$

Fluctuations of the angle of arrival of a wave are directly proportional to fluctuations in phase when both the viewing aperture and angle of arrival are small. Figure 4 shows a wave incident on a circular aperture of diameter  $\rho$ . The diameter is small enough so that the lines of constant phase are straight across the entire opening. The angle of arrival  $\theta$  is a consequence of the tilt of the wavefront acquired by traveling through turbulence. When  $\theta \ll 1$  the change in phase  $\Delta S$  of the wavefront across the aperture is

$$\Delta S = S(\rho_1) - S(\rho_2) = k\rho \sin \theta \approx k\rho\theta. \quad (2)$$

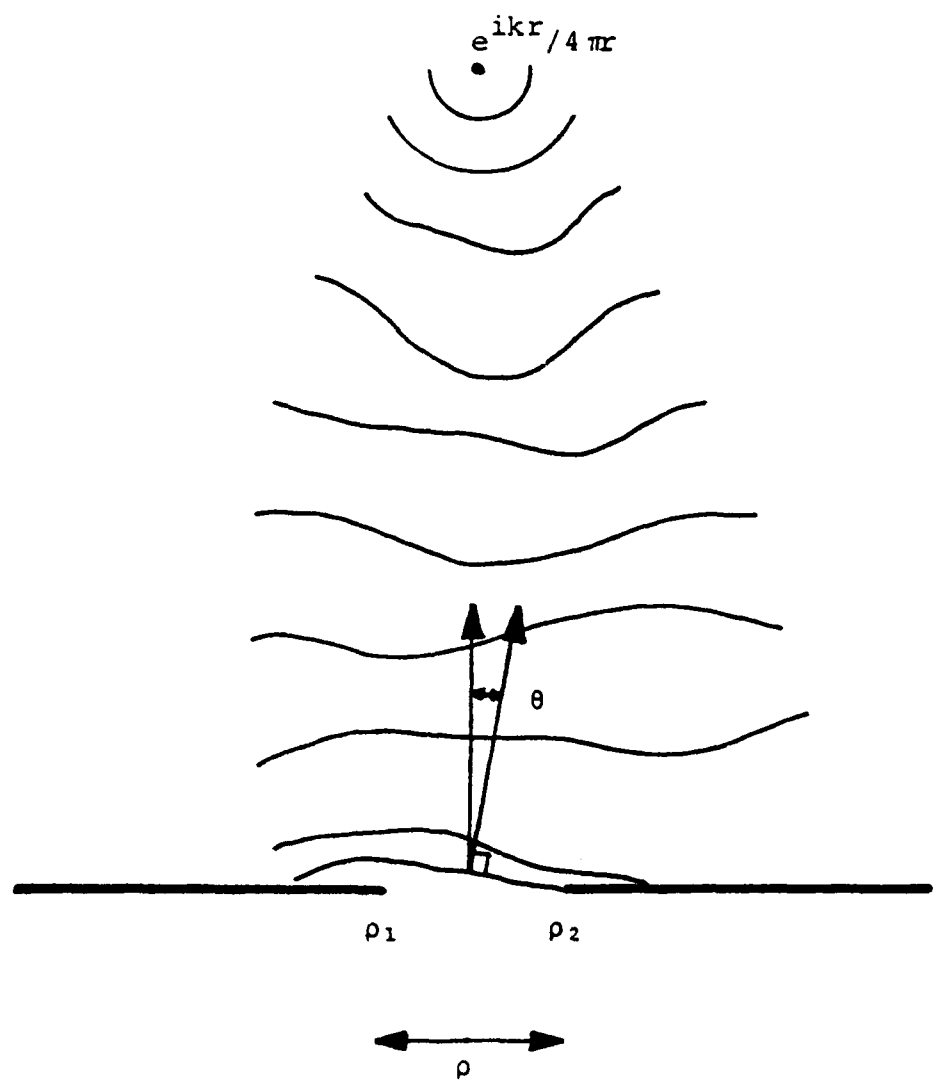


Figure 4: Turbulence induced wave tilt of backscattered light.

where  $k = 2\pi/\lambda$  is the wave number.

Since  $S$ , and therefore  $\theta$ , are random variables, we are only interested in statistical quantities. For example, the variance of the angle of arrival is

$$\langle \theta^2 \rangle = \frac{\langle (\Delta S)^2 \rangle}{k^2 \rho^2} = \frac{D_S(\rho)}{k^2 \rho^2} \quad (3)$$

where  $\langle \dots \rangle$  denotes an ensemble average.

In Eq. 3  $D_S$  is recognized as the phase structure function from turbulence theory and is a function of  $C_n^2$ . The choice of  $D_S$  is dependent on the parameter regime of the turbulence, the form of the free space wave (the wave in the absence of turbulence), and the spatial spectral power density of the index of refraction fluctuations.

The phase structure function appropriate for our situation is that for a spherical wave radiated from the origin [1]:

$$D_S(\rho, L) = 8\pi^2 k^2 \int_0^L dz C_n^2(z) \int_0^\infty \kappa d\kappa [1 - J_0(\kappa\gamma\rho)] \cos^2 \left[ \frac{L\gamma(1-\gamma)}{2k} \kappa^2 \right] \tilde{\Phi}_n(\kappa), \quad (4)$$

where  $\gamma = z/L$ ,  $z$  is the variable along the propagation path (assumed perpendicular to the plane of the aperture), and

$$\tilde{\Phi}_n(\kappa) = 0.033 \kappa^{-11/3} e^{-\kappa^2/\kappa_m^2}. \quad (5)$$

In Eq. 5  $\kappa_m = 5.91/l_0$ , where  $l_0$  is the inner scale length (typically 1 to 10 mm).  $\tilde{\Phi}_n$  is the spectral power density of the index of refraction fluctuations, divided by  $C_n^2(z)$ . We assume that the spectral density is a function of space only through the amplitude factor  $C_n^2(z)$ .  $\tilde{\Phi}_n$  is a modified Kolmogorov spectrum (modified by the factor  $e^{-\kappa^2/\kappa_m^2}$ ).

When  $C_n^2$  is constant and when  $\rho \gg \sqrt{\lambda L}$  then

$$\sigma_\theta^2 \approx \frac{1.0924 C_n^2 L}{\rho^{1/3}}. \quad (6)$$

This is the relation we use for our current experimental setup shown in figure 1.  $L$  is taken to be twice the distance from the transmitter to the focus.

## 6 Range resolved $C_n^2$

### 6.1 Forward and Backscattered Paths

In determining  $C_n^2$  along the laser path, we must give different consideration to the forward and backscattered paths, and to the distance between them. With the forward path we follow the same ray path as it wanders through the turbulent atmosphere, backscattering at each range as it travels. With the backscattered path we detect the ray path that happens to wander back to our detector. For each range there is a different backscattered path.

In addition, if there is nonzero correlation between the index of refraction fluctuations along the forward and backscattered paths, the change in propagation direction acquired along the forward path is partially negated along the backscattered path. When the paths are completely correlated, the change in propagation direction is unobservable by the receiver.<sup>1</sup>

For our proposed lidar system we cannot utilize the beam wander that occurs along the forward path. Since we observe the beam through the turbulent medium we cannot know where it wandered to. We must therefore devise a way to negate the effects of the forward path beam wander in our measurements. This is easily done by having two (spatially separated) receivers which measure, for each range, the angles of arrival for two paths backscattered from the beam. We then consider the variance of the difference of these angles of arrival:

$$\begin{aligned}\langle(\theta_1 - \theta_2)^2\rangle &= \langle\theta_1^2\rangle + \langle\theta_2^2\rangle - 2\langle\theta_1\theta_2\rangle \\ &= 2\langle\theta^2\rangle - 2\langle\theta_1\theta_2\rangle \\ &= 2\langle\theta^2\rangle(1 - \varrho)\end{aligned}\tag{7}$$

where we have recognized that for homogeneous turbulence  $\langle\theta_1^2\rangle = \langle\theta_2^2\rangle$ . In Eq. 7  $\varrho$  is the correlation between the two downward paths. For suitable separation between the two receivers we will show this to be negligible.

We have developed two methods for determining  $C_n^2$  along the beam path from angle of arrival fluctuations. The bending moment method is applicable to the

<sup>1</sup>Strictly speaking, this assumes the forward and backscattered free space electromagnetic waves are the same. We assume spherical waves in both cases.

forward path while the deconvolution method is applicable to the backscattered path. Although we cannot use the bending moment method for our proposed lidar we will describe it since it is applicable to other situations where the exact location to which the beam has wandered is known.

The two methods differ in the order in which data from individual laser shots are summed and processed. The deconvolution method processes after summing. The bending moment method processes before summing. The bending moment method is simpler and faster than the deconvolution method. In addition, uncertainty in the measurement is not amplified in the process of computing  $C_n^2$ . In the deconvolution method uncertainty in the measurement is amplified. The bending moment method is the preferred method if it is applicable to the experiment.

## 6.2 Deconvolution method

### 6.2.1 Description

With the deconvolution method we solve for  $C_n^2(z)$  by writing Eqs. 3 to 5 as a matrix equation and inverting. Equations 3 to 5 can be written in the following form:

$$M(L) = \int_0^L dz C(L-z) G(z, L), \quad (8)$$

where  $M(L)$  denotes the measured quantity,  $C(L-z)$  is the unknown to be determined, and the kernel  $G(L, z)$  is a known function. Here we imagine the receiver, at  $z = 0$ , detecting the angle of arrival on axis of a spherical wave radiating from a distance  $L$  away. The variability of  $L$  denotes the fact that the source, which is the atmospheric backscatter, moves away from the detector during each laser pulse. Since the integral is performed from the source at  $z = L$  to the receiver at  $z = 0$  the unknown  $C$  must vary from  $C(L)$  to  $C(0)$ .

For discrete distances, Eq. 8 can be written as a matrix equation:

$$\begin{pmatrix} M_0 \\ M_1 \\ M_2 \\ \vdots \\ M_n \end{pmatrix} = \Delta z \begin{pmatrix} G_{00} & 0 & 0 & \cdots & 0 \\ G_{10} & G_{11} & 0 & \cdots & 0 \\ G_{20} & G_{21} & G_{22} & \cdots & 0 \\ \vdots & \vdots & \vdots & \ddots & \vdots \\ G_{n,0} & G_{n,n-1} & G_{n,n-2} & \cdots & G_{n,0} \end{pmatrix} \begin{pmatrix} C_0 \\ C_1 \\ C_2 \\ \vdots \\ C_n \end{pmatrix} \quad (9)$$

The inversion of Eq. 9 is straightforward because the kernel is a lower triangular matrix:

$$\begin{aligned} C_0 &= \frac{M_0}{G_{00}\Delta z} \\ C_k &= \frac{M_k - \sum_{i=0}^{k-1} G_{k,k-i} C_i \Delta z}{G_{k0}\Delta z} \quad (k = 1, 2, \dots, n) \end{aligned} \quad (10)$$

### 6.2.2 Examples

Figure 5 shows a sample calculation of the deconvolution method. A model  $C_n^2$  profile typical of the atmosphere is assumed.[2] Values of  $\sigma_\theta^2$  are calculated with Eq. 9. Values of  $C_n^2$  are then regenerated using Eq. 10.

We see that in the absence of uncertainty in the measurements the deconvolution method can regenerate the  $C_n^2$  profile exactly. That is, the deconvolution method is numerically stable. The deconvolution method is however quite sensitive to uncertainty in the measured data. We will discuss this further below when we calculate minimum measureable  $C_n^2$  as a function of system parameters.

## 6.3 Bending moment method

### 6.3.1 Description

In the bending moment method we recognize the fact that the change in the direction of propagation at a particular point along the path is only dependent on the value of  $C_n^2$  at that point. By calculating the change in propagation direction along the path from the measured values of angle of arrival we can determine  $C_n^2$  directly, without having to integrate over all angles of arrival previous to the point in question.

When the deviation of the beam from the axis is small its trajectory can be written as

$$\vec{r} = [x(z), y(z), z], \quad (11)$$

where  $z = ct$  is the propagation direction and  $x$  and  $y$  are two directions orthogonal to each other and to  $z$ . The observed angles of deviation  $\theta_x$  and  $\theta_y$  of the trajectory from the axis are then  $x/z$  and  $y/z$  respectively.

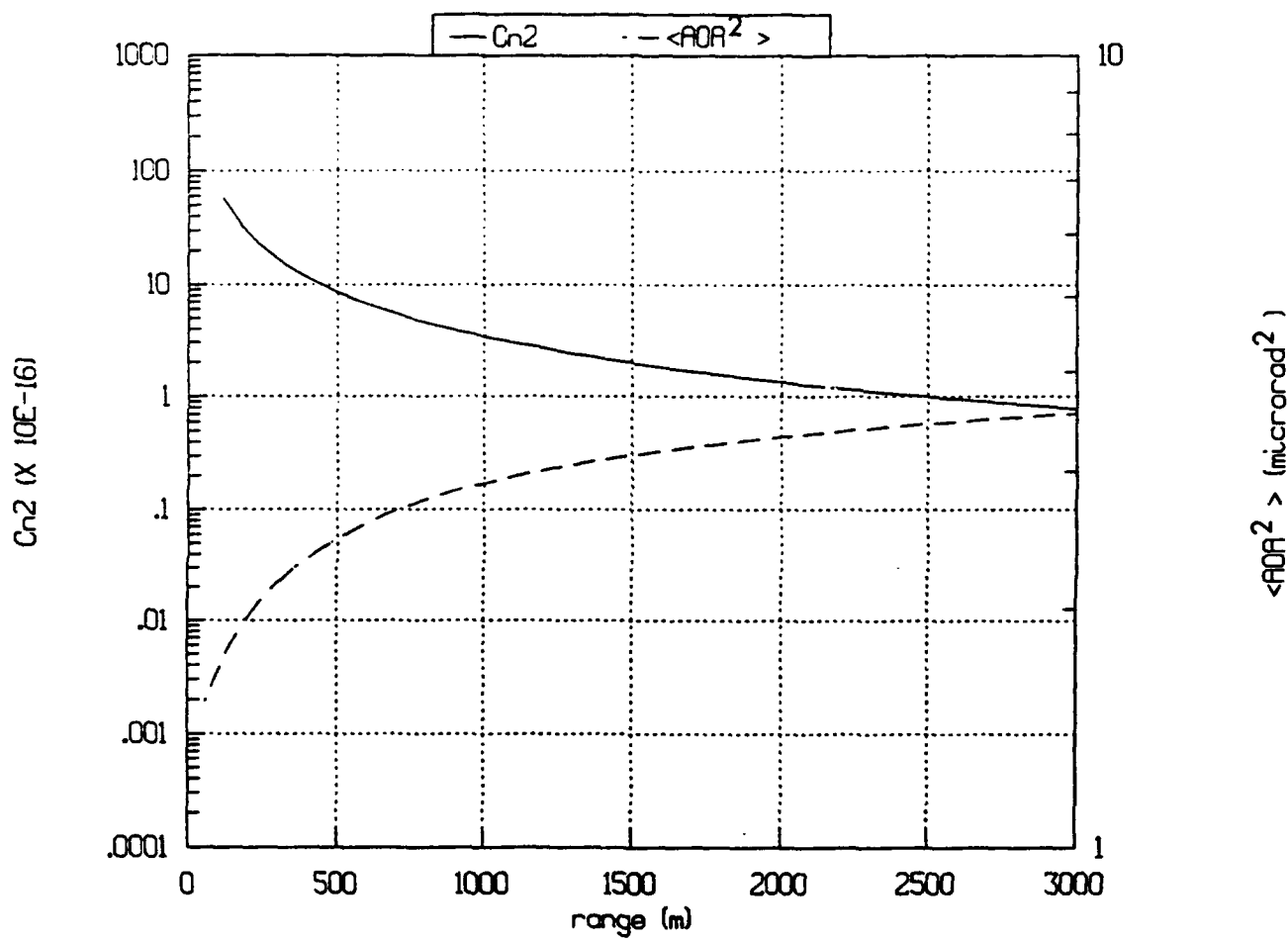


**Figure 5:** Deconvolution method sample calculation with  $C_n^2(z) \propto z^{-4/3}$ . The retrieved and model  $C_n^2$  profiles are the same. "AOA" means angle of arrival.

The tangent vector of the trajectory is

$$\vec{r}' \approx [x'(z), y'(z), 1], \quad (12)$$

where the prime indicates differentiation with respect to  $z$ . The angles between the tangent vector and the  $z$  direction are

$$\begin{aligned} \alpha_z &= \theta_z + z\theta'_z \\ \alpha_y &= \theta_y + z\theta'_y. \end{aligned} \quad (13)$$

The connection to turbulence theory is through the changes of the angles  $\alpha_{z,y}$  over a short section of path over which  $C_n^2$  is constant. From Eq. 6 we expect that

$$\langle |\Delta\alpha|^2 \rangle = \frac{1.0934 C_n^2(z) \Delta z}{\rho^{1/3}}, \quad (14)$$

where  $\Delta z$  is the length of the short section of path,  $\rho$  is the beam diameter, and

$$\begin{aligned} |\Delta\alpha|^2 &= \Delta z (\alpha_z'^2 + \alpha_y'^2) \\ &= \Delta z [(2\theta'_z + z\theta''_z)^2 + (2\theta'_y + z\theta''_y)^2] \end{aligned} \quad (15)$$

$\langle |\Delta\alpha|^2 \rangle$  is the variance of this quantity calculated from measurements of  $\theta(z)$  for many laser pulses. If motion is observed only in one direction, ( $\theta_z$  for example) we can simply double the result for that axis:

$$\langle |\Delta\alpha|^2 \rangle = 2\Delta z \langle (2\theta'_z + z\theta''_z)^2 \rangle. \quad (16)$$

The question of stability for this method does not apply since we calculate  $C_n^2$  on a point by point basis. There will be some amplification of uncertainties because derivatives of  $\theta$  are needed to get  $C_n^2$ . Unlike the deconvolution method however, these amplified uncertainties are not cumulative along the path.

### 6.3.2 Examples

Figures 6a and 6b show a sample calculation for beam wander in one dimension. The model  $C_n^2$  profile used in figure 5 is used here. Values of  $\Delta\alpha(z_i)$  are calculated for 100 laser pulses with a random number generator that generates Gaussian random variables with mean zero and variance given by Eq. 14.  $z_i$  takes on values from 30 m to 3000 m in steps of 30 m. Values of  $\theta(z_i)$  are then calculated for each laser pulse using a finite difference version of Eq. 15. These values of  $\theta(z_i)$ , now considered the measured values, are used in Eqs. 14 and 15 to regenerate  $C_n^2$ .

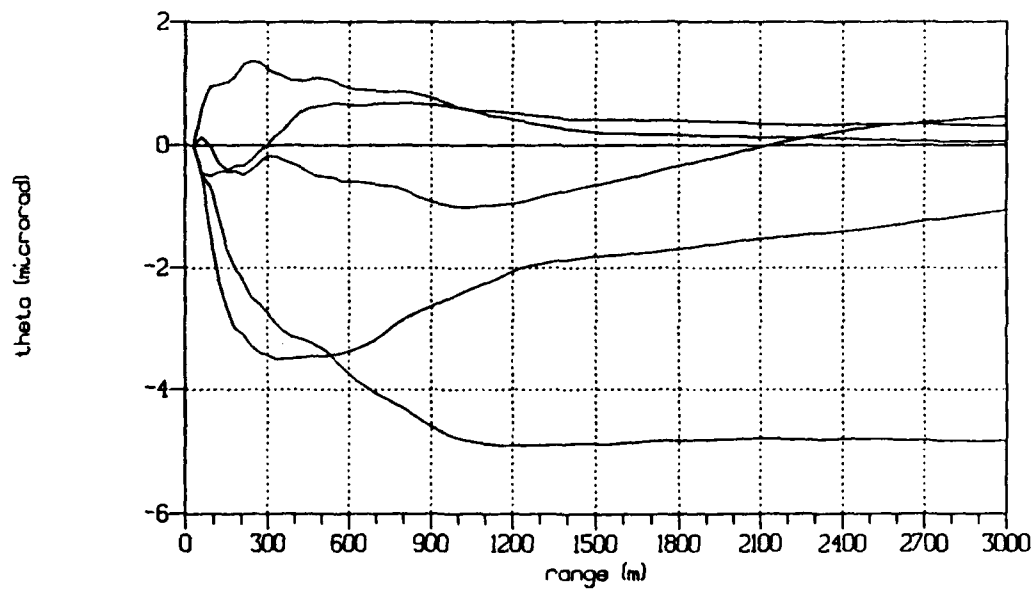
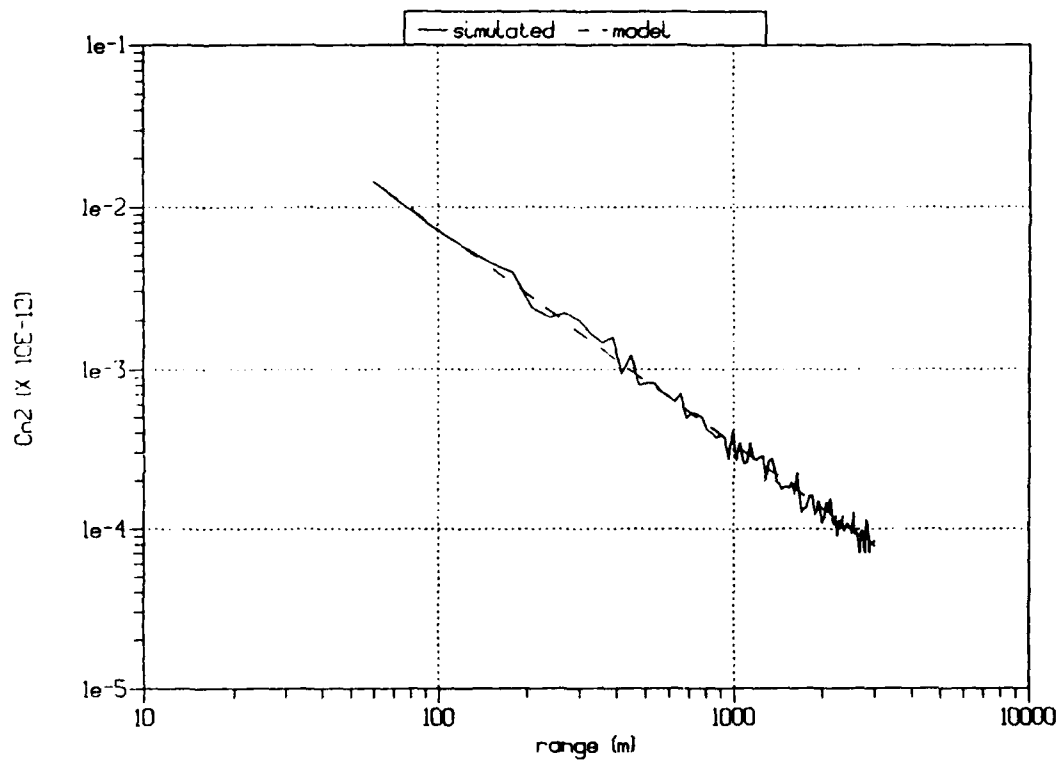


**Figure 6:** Bending moment method sample calculation for 100 laser pulses with  $C_n^2(z) \propto z^{-4/3}$ . a) Generated and actual  $C_n^2(z)$ . b) Simulated  $\theta(z)$  for five laser pulses.

## 6.4 Errors and Uncertainties

There are three sources of uncertainty in our technique for determining  $C_n^2$  from angle of arrival measurements which are independent of any particular system. They are

1. finite number of measurements,
2. nonzero spot size, and
3. correlation of paths.

We will discuss each of these separately and determine the minimum measureable  $C_n^2$  of our technique.

### 6.4.1 Statistical Nature of Turbulence Model

Since the turbulence model we use assumes from the outset that turbulence is random (i.e. the index of refraction fluctuation is a random variable), it is only useful in describing statistical quantities. Therefore, any finite number of measurements of a particular parameter will have uncertainty.

The angle of arrival  $\theta_i(z)$  of the light from the  $i^{th}$  laser pulse backscattered from range  $z$  is a random variable described by a Gaussian probability density function with mean zero and variance  $\sigma^2(z)$  given by Eq. 3. The estimate of the variance of  $\theta(z)$ , given by

$$\langle \theta^2(z) \rangle = \frac{1}{N} \sum_{i=1}^N \theta_i^2(z),$$

formed from  $N$  independent measurements of  $\theta$ , is a random variable described by a gamma probability density function with mean  $\sigma^2(z)$  and variance  $2\sigma^2(z)/N$ . Since  $C_n^2$  is proportional to  $\sigma^2(z)$ , we have the usual result that the fractional error in  $C_n^2$  is proportional to  $N^{-1/2}$ . Therefore, uncertainties due to the statistical nature of turbulence can in principle be reduced to arbitrarily small values by averaging over enough laser pulses. (Of course, this is limited by the condition that the measurement be made while  $C_n^2$  is not changing.)

### 6.4.2 Nonzero Spot Size

We cannot measure the exact location of the wandering beam because the backscattered wave does not really come from a point, as we have been assuming. The backscattered wave comes from a spot. The spatial extent of the spot depends on the laser beam spread (due to the diffraction limit of laser beam optics and turbulence induced beam broadening) and on the diffraction limit and aberrations of the receiver optics.

For our calculations of  $C_n^2$  we need to determine the average position, or the centroid, of the spot. We expect the photons of the spot to be randomly distributed, described by a two dimensional Gaussian probability density function. The mean of the Gaussian is the theoretical position of the centroid (i.e., the position detected if the spot were a point or if there were an infinite number of photons in the spot). The variance (the square of the uncertainty in position of the spot) is the sum of the variances of all processes which cause the spot to have nonzero angular extent, divided by the number of photons. That is, the variance, expressed in terms of the angular extent of the spot as viewed by the receiver is

$$\sigma_s^2 = \frac{(1.22\lambda/d)^2 + [w(z)/z]^2}{M(z)} \quad (17)$$

where,  $d$  is the receiver aperture diameter,  $M$  is the number of photons received, and  $w$  is the laser beam width. In Eq. 17 we have assumed the receiver to be diffraction limited and we have noted that both  $M$  and  $w$  are functions of range.

In Eq. 17 we have also neglected turbulence induced beam broadening and beam breakup (temporally this corresponds to scintillation or speckle). We assume the major effect of turbulence is beam wander (we feel this is borne out by our experiments described in Section 4). For very long propagation lengths beam breakup becomes more severe. In this regime the weak turbulence theory we describe in Section 5 is no longer applicable and we must consider strong turbulence theory.

For a single mode, Gaussian laser beam, the beam width is given by

$$w^2(z) = w_o^2 + \frac{16\lambda^2}{\pi^2 w_o^2} (z - z_o)^2, \quad (18)$$

where  $w_o$  is the beam width at the beam waist, located at position  $z_o$  from the laser.

Nonzero spot size places a lower limit on the value of  $C_n^2$  that we can measure. Unlike the uncertainty due to the random nature of turbulence, this lower limit does not diminish by averaging over more laser pulses.

#### 6.4.3 Correlation of paths (Isoplanatism)

We have mentioned that nonzero correlation between the upward and downward paths partially negates the observation of beam wander experienced by the upwardly propagating beam. Similarly, the variance of the difference in angles of arrival between two spatially separated backscattered paths, as shown in Eq. 7, is not simply the sum of the variances of each angle of arrival if the paths are correlated. This effect is known as isoplanatism.

The correlation  $\varrho(\vartheta, L)$  of two paths with angular separation  $\vartheta$  originating at a distance  $L$  away is

$$\varrho(\vartheta, L) = e^{-(\vartheta/\vartheta_o)^{5/3}}. \quad (19)$$

$\vartheta_o$  is known as the isoplanatic angle and is defined in reference [3] as

$$\vartheta_o = \left( 2.95k^2 \int_0^L z^{5/3} C_n^2(z) dz \right)^{-3/5} \quad (20)$$

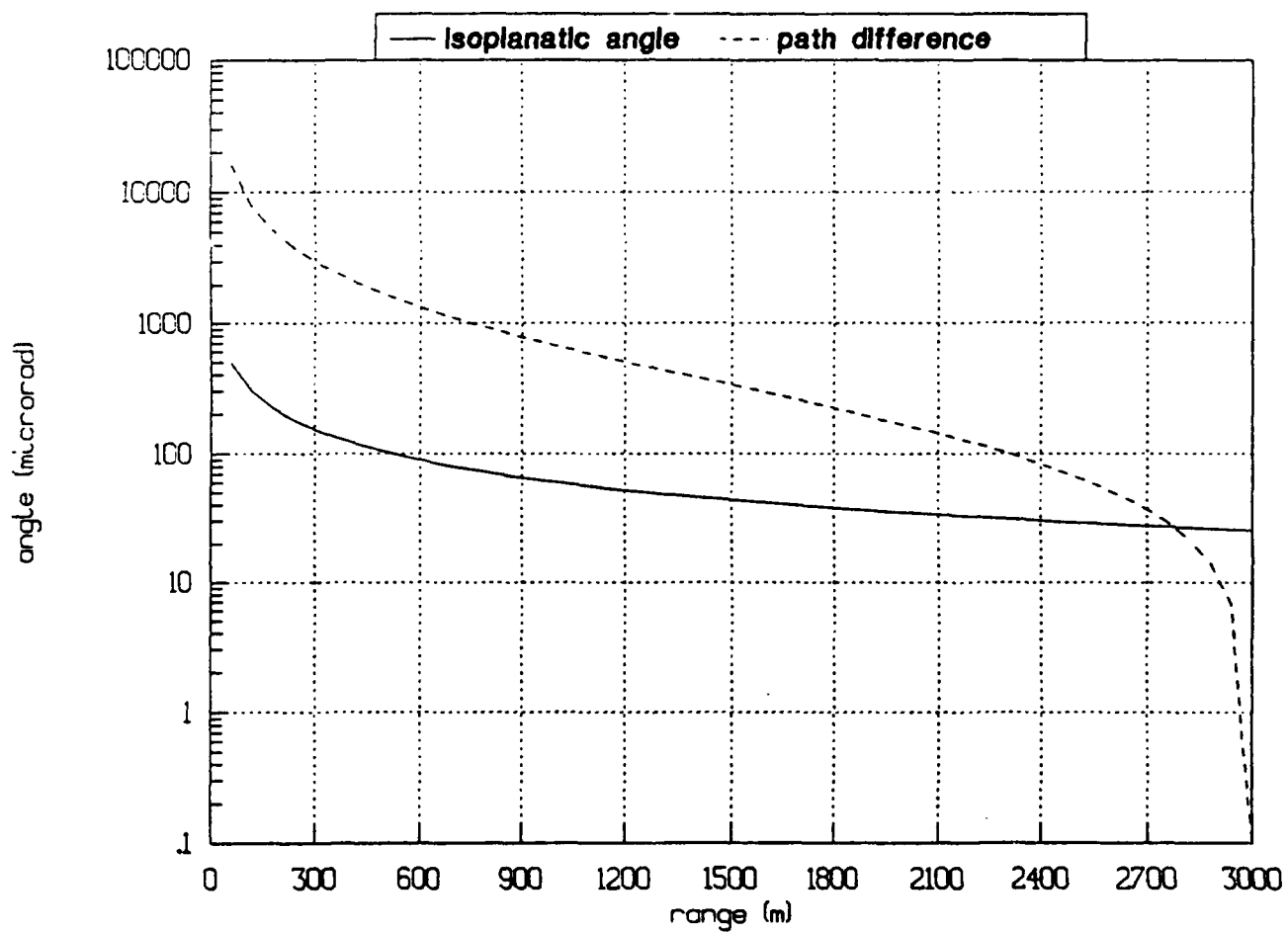
where  $k = 2\pi/\lambda$  is the wavenumber of the light.

Figure 7 shows the isoplanatic angle as a function of altitude for the  $C_n^2$  profile used in figure 5. Also shown is the angular separation (in the absence of turbulence) of the two paths backscattered from an altitude of 3 km to two receivers separated by 1 m. The farthest backscattered point is also the most highly correlated.

We incorporate path correlation into the expressions for angle of arrival and test its effect on our deconvolution technique. Using Eq. 7 the correlation is included in Eq. 8 in the following way:

$$M(L) = \int_0^L dz C(L-z) G(z, L) [1 - \varrho(L-z)] \quad (21)$$

That is, at each incremental distance along the path back to the receiver, the variance of the angle of arrival for each path is reduced by the factor  $[1 - \varrho(L-z)]$ . The correlation  $\varrho$  is given by Eqs. 19 and 20. The angular separation  $\vartheta$  between



**Figure 7:** Isoplanatic angle for  $C_n^2 = z^{-4/3} \times (10^{-18} \text{ m}^{2/3})$  and angular path difference of two paths backscattered from 3 km.

the two paths is a function of the distance  $z$  from the receiver and is given by

$$\vartheta(z) = \frac{L-z}{zL} h, \quad (22)$$

where  $h$  is the separation of the two receivers.

When the separation between the two receivers is 1 m there is negligible difference between calculations performed with and without correlation effects (for the  $C_n^2$  profile used in figure 5). The reason is because both the path separation and  $C_n^2$  are smaller closer to the point of backscatter (for a typical atmosphere with  $C_n^2$  decreasing with increasing altitude). Since the variance of the angle of arrival is a weighted integral over the entire backscattered path (weighted by  $C_n^2$ ), the region of higher correlation contributes less to the net variance in the angle of arrival.

This reasoning tells us that the variances are not greatly affected when isoplanatism is considered. However, the same reasoning says that incorporating isoplanatism into the inversion equation would make an already ill-posed problem even worse. That is because in the inversion we are dividing by the small values of the kernel near the backscattered point. These values are reduced further with the isoplanatism effects included. Therefore, the best we could hope for is to reduce isoplanatism effects rather than to incorporate them into our inversion technique.

#### 6.4.4 Minimum Measureable $C_n^2$

If we include the effects of uncertainty in spot size and finite number of shots into the deconvolution method for determining  $C_n^2$ , we can determine the minimum measureable  $C_n^2$  as a function of system parameters such as laser power, beam spread, aperture diameter, range, and receiver separation. System dependent uncertainties (such as detector resolution) will be discussed separately.

Figure 8 shows a sample calculation, similar to the one shown in figure 6, which includes the uncertainty in the spot centroid location, correlation, and finite number of shots. The same model  $C_n^2$  profile is used. The "theoretical" variances of the angles of arrival are calculated using Eq. 21, which has been corrected for isoplanatism. The distance between the two receivers is 1 m.

To incorporate spot location uncertainty and finite number of shot uncertainty, we add a random number to each of these variances before inverting. The random

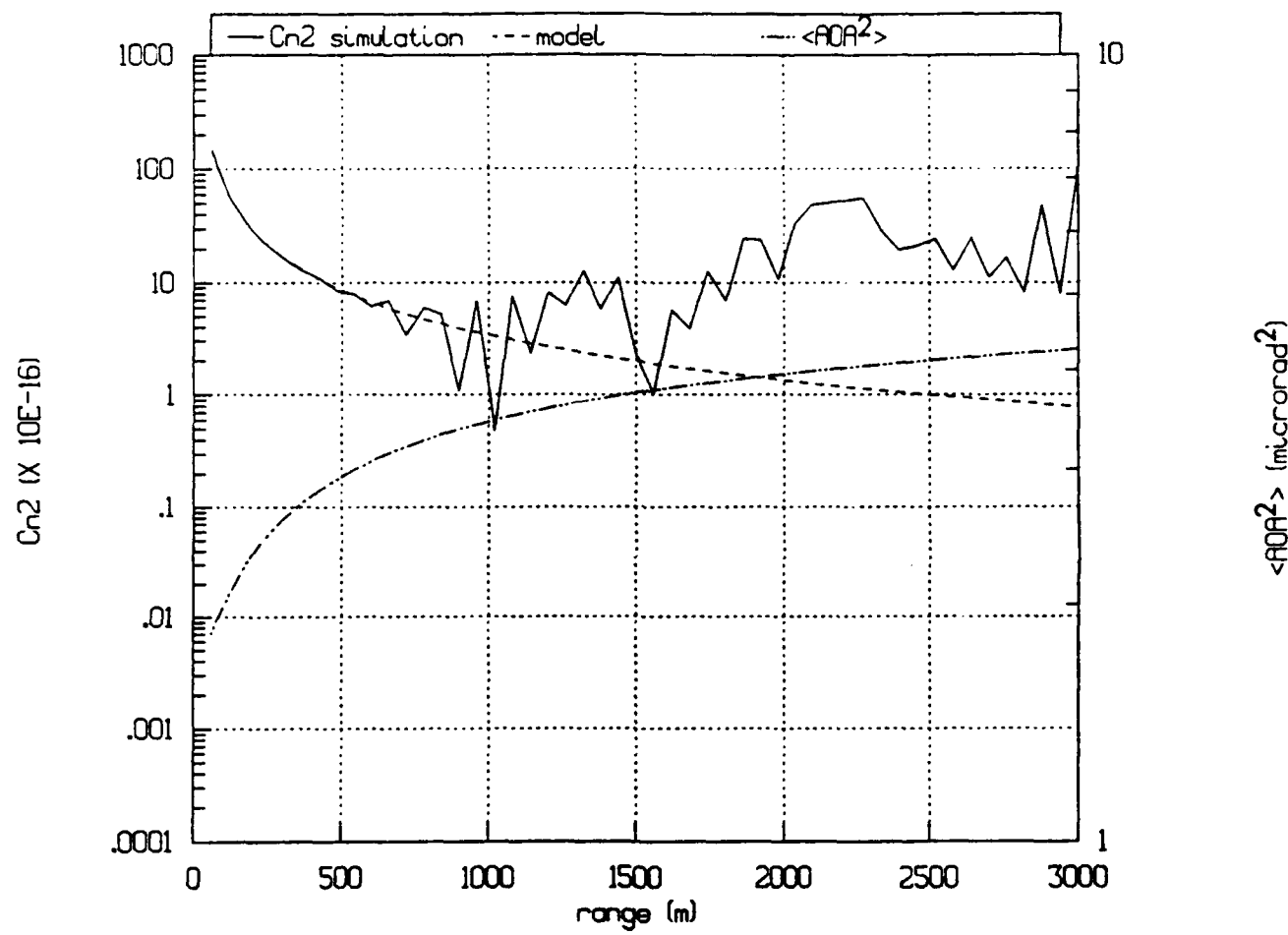


**Figure 8:** Sample calculation with  $C_n^2(z) \propto z^{-4/3}$ . A (ten times) Raleigh atmosphere is assumed. Spot centroid location uncertainty and isoplanatism are included.

number has a gamma probability distribution with mean  $\sigma_s^2$  given by Eq. 17 and variance equal to  $2\sigma_s^2/N$ , where  $N$  is the number of shots.

The number of backscattered photons in Eq. 17 is calculated with a Gaussian random number generator. The mean is given by the number of backscattered photons expected from an aerosol laden atmosphere having a conservatively chosen scattering cross section ten times the standard Rayleigh value for air. The variance is the number of photons. The probability distribution should be Poissonian, however, Gaussian is a good approximation for a large number of photons.

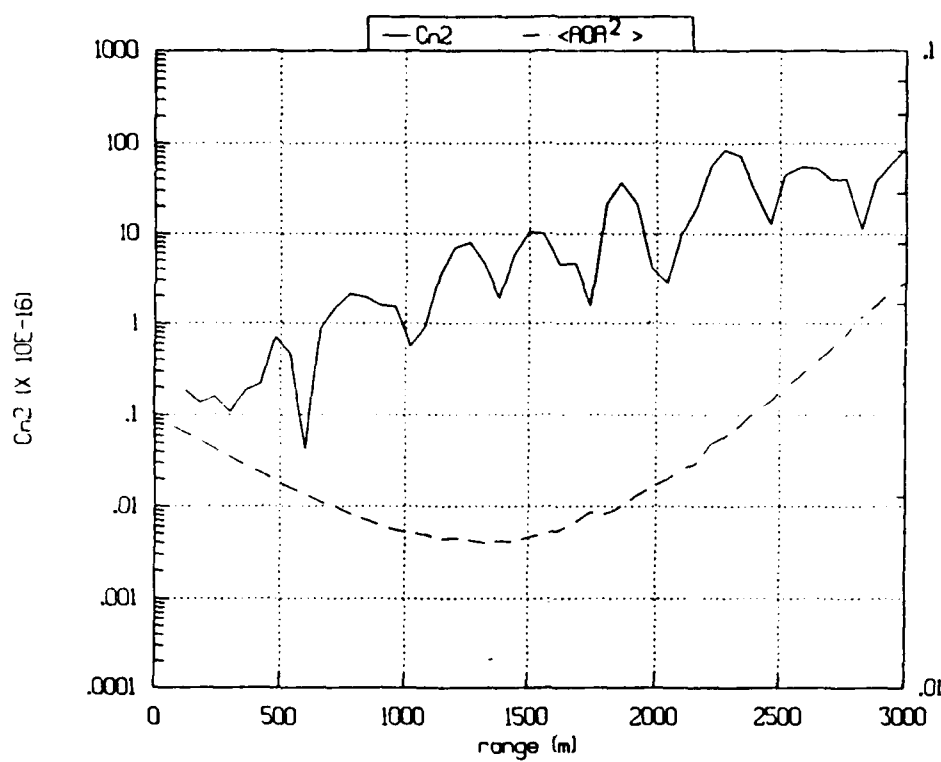
Other parameters for figure 8 are:

Laser energy: 1 J/pulse,  
wavelength: 532 nm,  
aperture diameter: 100 cm,  
range resolution: 60 m,  
beam waist location: 1500 m from laser output, and  
beam depth of field: 3000 m (i.e.  $w(z) = \sqrt{2}w_0$  for  $z = 0, 3000$ m).

Figure 8 shows that the simulated measurement accurately reflects  $C_n^2$  out to 1 km, after which it begins to deviate. The deviation is due primarily to the large uncertainty in spot location relative to the amount of beam wander produced by the small turbulence levels at high altitudes.

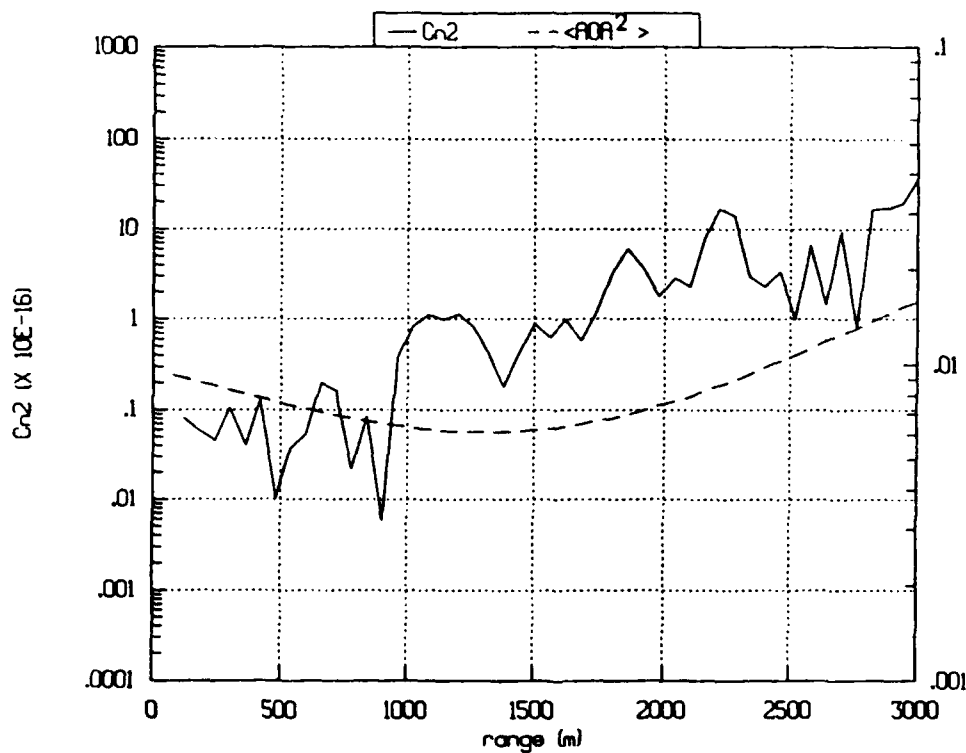
We can calculate the minimum measureable values of  $C_n^2$  for a given set of parameters by doing simulations with  $C_n^2 = 0$ . Figure 9 shows the difference between two cases with the same range resolution of 60 m but different aperture diameters (60 cm and 100 cm). Figure 10 shows the difference between two cases with the same aperture diameter of 60 cm but with different range resolutions (100 m and 200 m). Figure 11 shows the difference between two cases with the same aperture diameter of 100 cm but with different range resolutions (100 m and 200 m). The minimum measureable  $C_n^2$  values lie on the upper envelopes of the minimum measureable  $C_n^2$  plots shown in the figures.

The minimum measureable  $C_n^2$  is inversely proportional to laser energy. The relationship with other parameters is not known analytically because of the integral effect of the inversion routine.



a

$\langle \Delta R^2 \rangle$  (microrad $^2$ )



b

$\langle \Delta R^2 \rangle$  (microrad $^2$ )

Figure 9: Minimum measurable  $C_n^2$  versus range for 60 m range resolution and two aperture diameters: a) 60 cm and b) 100 cm.

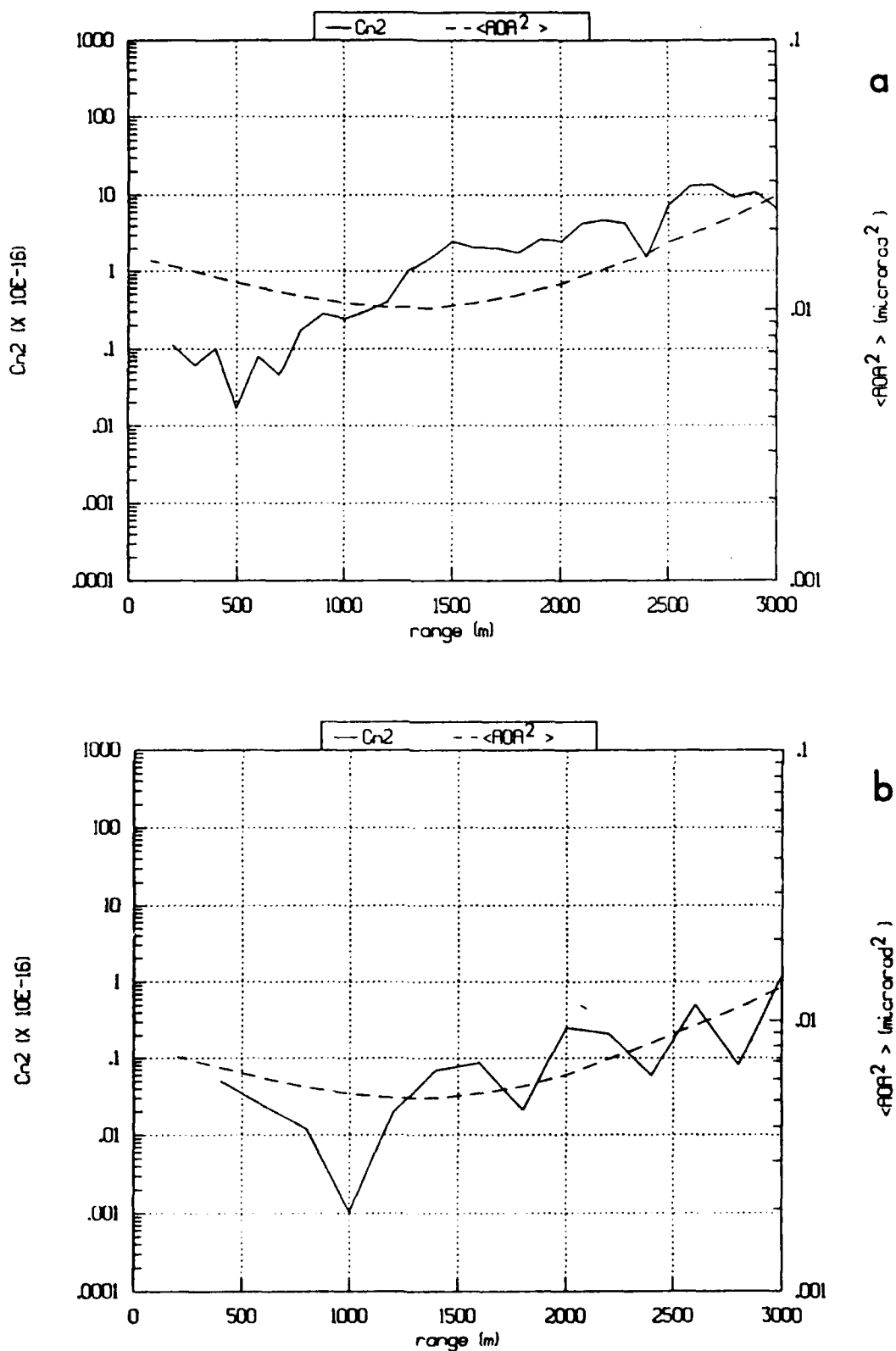
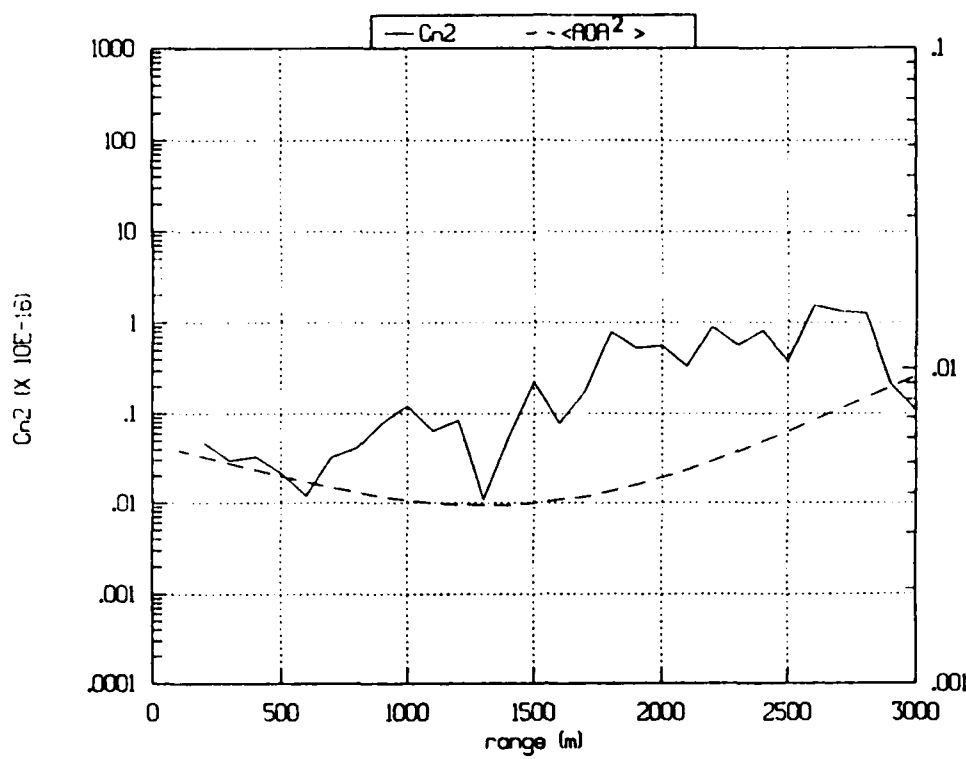
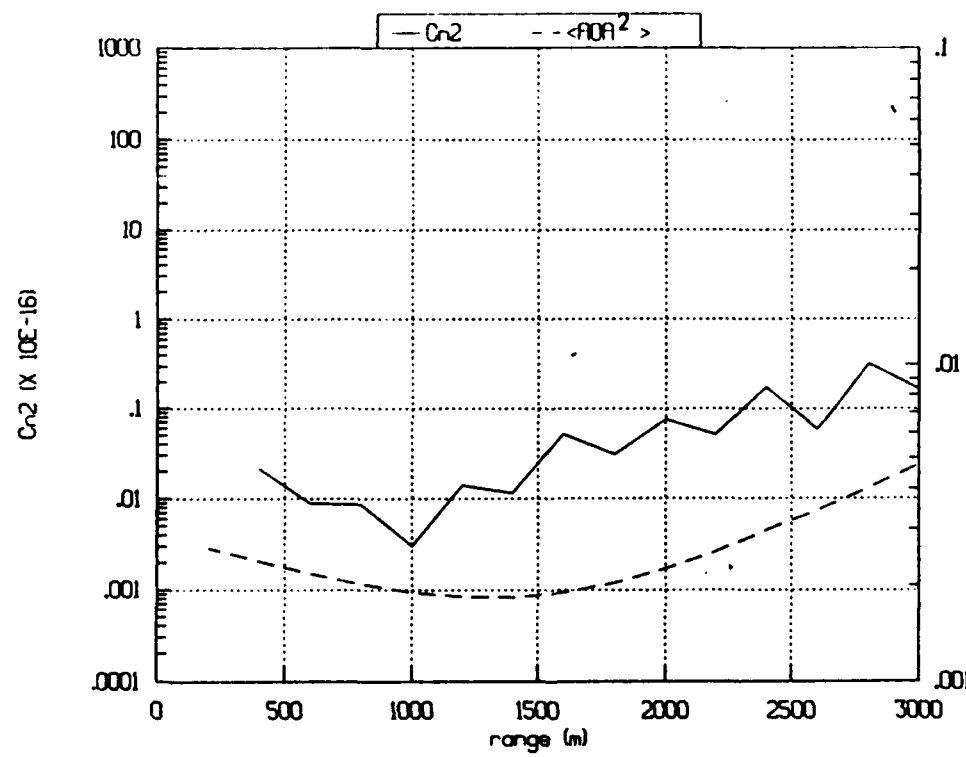


**Figure 10:** Minimum measurable  $C_n^2$  versus range for 60 cm aperture diameter and two range resolutions: a) 100 m and b) 200 m.



a



b

Figure 11: Minimum measurable  $C_n^2$  versus range for 100 cm aperture diameter and two range resolutions: a) 100 m and b) 200 m.

The figures show that the minimum measurable  $C_n^2$  is more sensitive to changes in range resolution than to changes in aperture diameter. The minimum measurable  $C_n^2$  is reduced by approximately a factor of ten by doubling the range resolution from 100 m to 200 m. It is only reduced by a factor of approximately two by increasing the aperture diameter from 60 cm to 100 cm.

The aperture diameter is fixed for a given system but the range resolution may be varied. In fact, it is possible to have lower resolution for farther ranges. Under typical atmospheric condition  $C_n^2$  changes more slowly at higher altitudes. Therefore, a lower range resolution, which is required due to the smaller backscattered signal, may be used.

## 7 Proposed Range Resolved System

### 7.1 Introduction

In this section we outline the design of a system which is capable of measuring  $C_n^2$  given by the model profile we have used in Fig. 8. Specifically, we are interested in a system capable of detecting  $C_n^2(3 \text{ km}) = 10^{-16} \text{ m}^{-2/3}$ .

Figure 10 indicates that a system with a 60 cm diameter receiver aperture, a 1 J/pulse laser, and 200 m range resolution can detect  $C_n^2 = 10^{-16} \text{ m}^{-2/3}$  at 3 km. With 100 m range resolution the same system can detect  $C_n^2 = 10^{-16} \text{ m}^{-2/3}$  at 1.5 km. A system with 100 m resolution for ranges less than 1.5 km and 200 m resolution for ranges between 1.5 km and 3 km would then meet our requirements.

Figure 12 is a diagram of the system. Below we summarize and describe the transmitter, receiver, and detector.

### 7.2 Transmitter

The transmitter consists of a single-spatial-mode, frequency-doubled, Q-switched Nd:YAG laser and a beam expanding telescope. The laser should produce 1 Joule per pulse at a repetition rate of at least 10 Hz. Single mode lasers at this energy have only recently become available with the development of the solid state injection seeder.

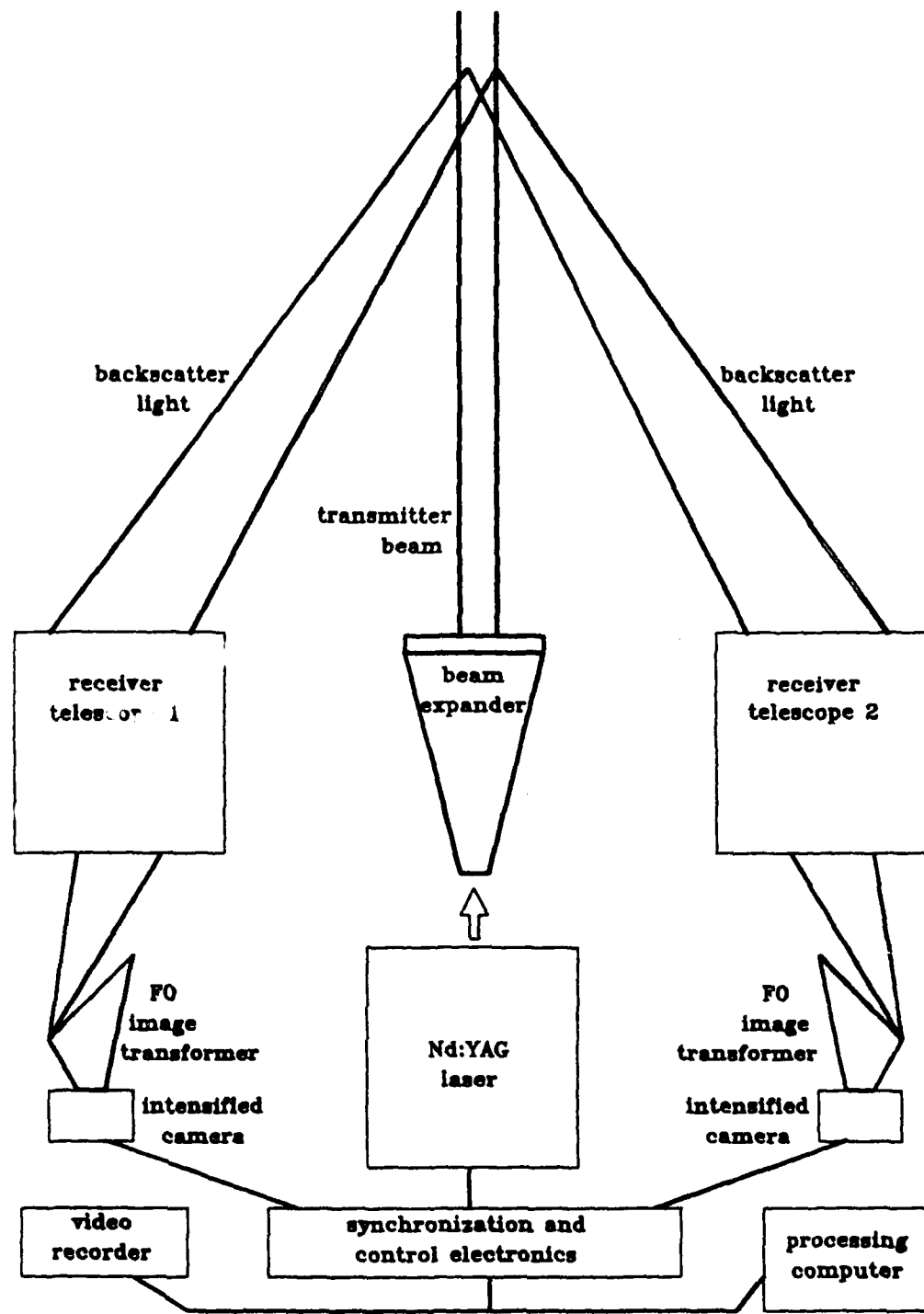


Figure 12: Proposed system.

The choice of doubled Nd:YAG was made by maximizing the predicted radiance of the backscattered image. This decision involved the energy, the wavelength, and the mode pattern. The usual Nd:YAG Q-switched pulse duration of 10 ns also places a reasonable lower limit on the range resolution of the lidar.

Our experimental simulation used a 14 cm diameter Newtonian beam expander made with simple singlet plano lenses. The laser spot diameter produced at 50 m was 4.5 times the diffraction limit. A long range system would need higher quality optics using best form singlets or even achromatic doublet lenses.

The proposed system has a diffraction limited, 3.2 cm diameter beam waist at 1.5 km range. The beam diameter at the exit of the expander and at 3 km is 4.5 cm. These beam diameters are measured at the  $1/e$  points. To avoid aperture diffraction effects, the diameter of the expander objective should be at least 7 cm.

A different concept for the transmitter, using a tilted slit arrangement is presented in section 7.4. This alternative can generate a narrower illuminated region, but it is unlikely to produce a higher irradiance. For this reason, we have rejected the tilted slit transmitter, but present it as a novel light source.

### 7.3 Receivers

Two receiver telescopes are proposed. They need to image microradian motions of the beam. They also have to collect as much light as is practical. We have chosen 60 cm for their diameters.

The focal lengths are determined by considering angular gain and off-axis aberrations. A focal length as short as 6 m ought to be obtainable without suffering significant image distortion.

A separation of one meter between the transmitter and the receiver telescopes has been shown to be adequate. The transmitter will probably be placed between the receivers. The two receivers will have to be connected to each other and to the transmitter. The relative alignment between the telescopes can not move by more than  $0.1\mu\text{rad}$ .

## 7.4 Tilted image plane

The resolution of the instrument will benefit by being focussed to the diffraction limit for each range of interest. Since these ranges are accessed simultaneously, a novel optical system will be needed. Such a system is realizable by placing a tilted image plane in the receiver telescopes.

Consider a straight line of light sources being imaged by a telescope of focal length  $f$ . The telescope axis is parallel to the line, and separated from it by distance  $d$ . The resulting image formed by the telescope will also be a line as shown in figure 13. The line forms an angle  $\alpha = \tan^{-1}(d/f)$  with the telescope axis, and extends from the infinity focus point.

If the light sources were not infinitesimally small point sources, but had width  $w$ , the width  $w_i$  of the image would be

$$w_i = \frac{wf}{z-f}. \quad (23)$$

The range from the receiver to the light source is  $z$ . For  $z \gg f$ , the image width is just proportional to the angular extent of the source. Since the image plane is inclined by angle  $\alpha$ , the image spots are stretched along the direction of the incline by  $1/\sin(\alpha)$ .

$$w_i/\sin(\alpha) = \frac{w(f^2 + d^2)^{1/2}}{z-f}. \quad (24)$$

For the design of the detector, we need to know where the light will strike the image plane. We will designate  $s$  as the distance along the inclined image plane. The infinity focus is at  $s = 0$ .

$$s = \frac{f(f^2 + d^2)^{1/2}}{z-f} \sim \frac{f^2}{z}. \quad (25)$$

By the reciprocity principle, one can place the line of light sources at the image end of the telescope and project a line of narrow foci into the atmosphere. The angular extent of the projected beam is just the width of the light sources divided by  $f$  (provided  $z \gg f$ ).

By this technique, one can project a beam whose width versus distance is not given by the usual diffraction formulas. The trick is that this "beam" is not really a beam, but the locus of many focal points.

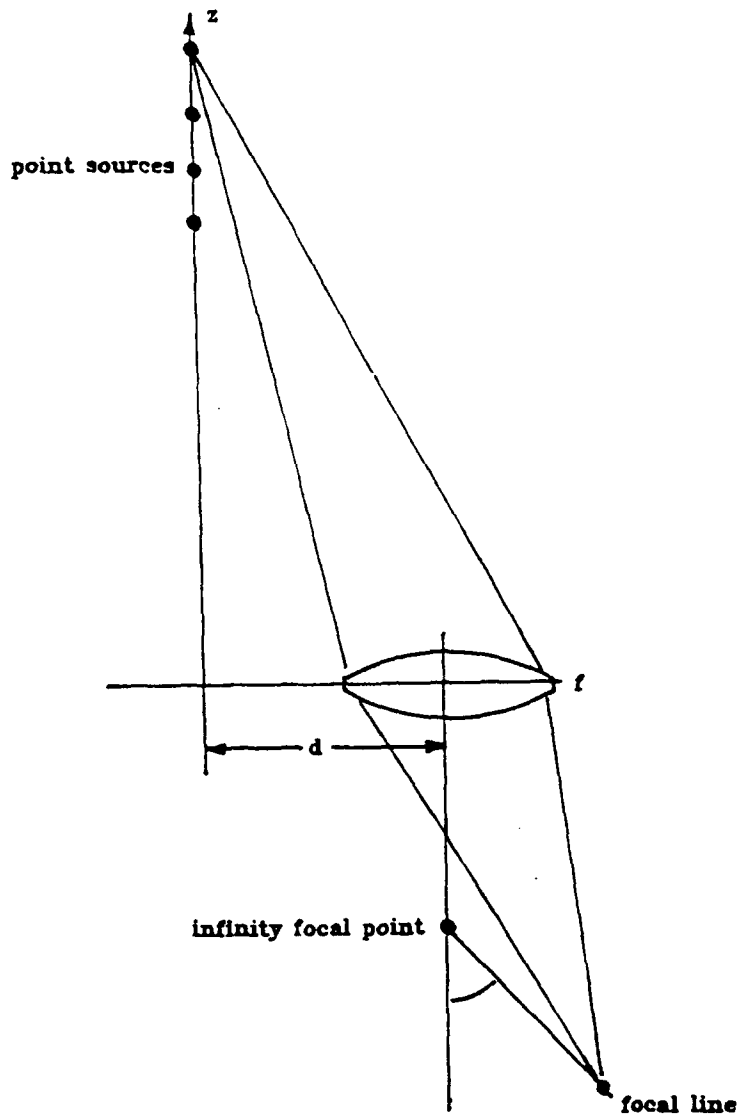


Figure 13: Tilted image plane telescope.

A potential experimental configuration has two such telescopes sharing a common beam line. The perpendicular separations from the line to the telescopes form a right angle. One of the telescopes transmits the laser light, and the other receives the backscatter. The laser light is shaped into a tilted line pattern using cylindrical optics and a slit before admission into the transmitter telescope.

As explained above, the backscatter from the line projected from the transmitter will image to a narrow line by the receiver telescope. A linear detector array can record the image, and angular deviations (along the axis of the array) of the beam can also be measured.

We should note that the modeling work and the proposed lidar system do not incorporate the tilted slit transmitter, but do use the tilted image plane receiver. Instead, the waist of a diffraction limited transmitter beam is placed half-way to the maximum measurement range with the depth-of-focus covering the entire range. This arrangement minimizes the average transmitter diameter over the range. While noticeably differing from the ideal diffraction limited point source, this beam provided a serviceable transmitter without the need for a tilted slit.

The tilted slit transmitter is avoided for reason of signal strength. The need to distribute the laser light along the transmitter slit diminishes the irradiance at each range. This diminution of irradiance cancels some or all of the gain in ability to precisely ascertain the centroid positions of the backscattered images.

## 7.5 Detectors

Time delay usually provides range information in a lidar system. Instead, we are proposing a parallax technique for the turbulence lidar. Since imaging detectors are needed to measure the beam wander, matters can be simplified considerably by not additionally requiring the detectors to have 100 ns time response.

First, we need to show that the detectors can have sufficient range resolution using parallax. By taking the derivative of equation 25, we can determine the incremental change in image position  $\Delta s$  per change in range  $\Delta z$

$$\Delta s = -\frac{f(f^2 + d^2)^{1/2}}{(z - f)^2} \Delta z. \quad (26)$$

If we set this equal to the inclined image spot size, given by equation 24, the resulting value of  $\Delta z$  is the minimum resolvable range increment:

$$\Delta z = (z - f)w/f \sim zw/f. \quad (27)$$

The range resolution increases with range, and has a value of 22.5 m at 3 km range for the proposed system. The system model used a range resolution of 100 m, so parallax is clearly sensitive enough. Both detectors would be allowed to record the return from all ranges for each laser shot before reading the images out to a computer.

The dimensions of the imaging detectors are rather unusual, however. Using equation 25, the length of each detector has to be 10.8 cm to detect the returns from 300 m through 3 km. The length increases rapidly as the minimum range is reduced. The detector width is only 90 to 130  $\mu\text{m}$  for most the most distant half of the range, however. At 300 m range, the spot has grown to 900  $\mu\text{m}$ .

Such a long, narrow stripe is not a common geometry for a low-light-level imaging detector. To couple this geometry to a more conventional detector, we can transform the image using a coherent fiber bundle. The fibers can be arranged to fill a 1 mm wide stripe at the image end of the bundle, and form a 1 cm by 1.1 cm rectangle at the detector end. The fiber bundle can even be stacked staircase fashion at the image plane to create the incline while still pointing along the axis of the telescope.

Finally, the detectors themselves can be microchannel plate intensifiers and CID arrays. The image information would be available every 33 ms as a video raster scan signal. The timing of the clearing and read out of the arrays can be modified to match the timing of the laser pulses.

### 7.5.1 Detector Resolution

For the system to be effective, the detector has to be capable of providing information about sub-microradian motions of the beam. It may seem, at first glance, that the detector pixels therefore have to be correspondingly small. This is not the case.

A statistical treatment of the error in the determination of the spot centroid reveals that it is sufficient for the pixel size to be somewhat smaller than spot. A

conservative value of three or more pixels per spot diameter will insure that the resolution is limited only by the number of photons collected.

### 7.6 Processing electronics

The processing can be done by capturing each laser shot image with a video frame grabber connected to a fast 80386 based computer. The computer can calculate the centroid at each altitude, smooth the data where necessary, and determine  $C_n^2(z)$  using the deconvolution technique explained in section 6.

Transmission of data in video format offers an advantage for data storage. A video recorder can buffer the data, reducing the speed requirement on the processing computer.

## 8 Conclusions

We have presented the design of a lidar system capable of remotely measuring range-resolved atmospheric turbulence by measuring the angle of arrival of the backscattered laser light. We have shown that a value for  $C_n^2$  of  $10^{-16} \text{ m}^{-2/3}$  at 3 km vertical range is measureable. A system capable of performing this measurement would require a 1 J/pulse laser and a 60 cm diameter receiver aperture. The required range resolution is 100 m for ranges less than 1.5 km and 200 m for ranges greater than 1.5 km.

The results of experiments using a fixed focus lidar have been presented. These experiments demonstrate the feasibility of measuring the angle of arrival of backscattered laser light.

We have developed a technique to calculate  $C_n^2$  as a function of range from angle of arrival measurements. We have used this technique to test the performance of hypothetical lidar systems.

## References

- [1] A. Ishimaru, *Wave Propagation and Scattering in Random Media, Vol. 2*, Academic Press, New York (1978).
- [2] J.C. Kaimal, J.C. Wyngaard, D.A. Haugen, O.R. Cote, and Y. Izumi, "Turbulence Structure in the Convective Boundary Layer," *J. Atmos. Sci.* **33**, 2152-2169 (1976).
- [3] D.L. Fried, "Anisoplanatism in Adaptive Optics," *J. Opt. Soc. Am.* **72**, 52-61 (1982).